An RBF–MFS model for analysing thermal behaviour of skin tissues

Leilei Cao [a,b], Qing-Hua Qin [b,*], Ning Zhao [a]

[a] *School of Mechatronics, Northwestern Polytechnical University, Xi'an 710072, PR China*
[b] *Department of Engineering, Australian National University, Canberra, ACT 0200, Australia*

ARTICLE INFO

ABSTRACT

A meshless model based on radial basis function and method of fundamental solution (RBF–MFS) is developed to investigate bioheat transfer problems. First, A time-stepping θ-method is used in handling the time variable in the Pennes bioheat equation. Then, the particular solution is approximated by a linear combination of radial basis functions, and the homogeneous solution is approximately determined by the method of fundamental solution. The multi-subdomain RBF–MFS technique is implemented for analysing problems containing different materials and/or multi-connected regions. The efficiency of the proposed method is assessed by several examples including normal tissue, tissue with tumor and burned tissue.

© 2009 Elsevier Ltd. All rights reserved.

1. Introduction

Thermal methods of temperature measurement at the skin surface, which require solutions of generalized bioheat equations under various specific internal and boundary conditions to simulate the real case, are becoming recognized as more attractive than other non-invasive thermometry like MRI, microwave and ultrasound [1] because they are more economic and safer[2]. Research on the prediction of living tissue temperature has developed continuously since the Pennes equation was proposed in 1948 [3]. Numerical methods used to solve the Pennes equation have included the finite difference method (FDM) [4–6], finite element method (FEM) [7–11], boundary element method (BEM) [12,13], dual reciprocity boundary element method (DRMBEM) [2,14] and Monte Carlo method (MCM) [15,16]. In addition, the Trefftz FEM [17,18] and meshless method [19] have also been successfully used to solve transient heat conduction problems. Among the above methods, the major drawback of FDM appears to be in its inability to handle effectively the solution of problems over arbitrarily shaped complex geometries because of interpolation difficulties between the boundaries and the interior points in order to develop finite difference expressions for nodes next to the boundaries. FEM is widely used because it can manage complex shapes well, but its main disadvantage is that it requires domain discretization which is time-consuming. BEM involves discretization of the boundary only, which is an important advan-

tage over FEM, but it has difficulty dealing with transient or non-homogeneous problems which still need domain discretization. Fortunately, DRMBEM can overcome this drawback by combining radial basis functions and conventional BEM to transform domain integrals to the boundary integral. An alternative numerical method is MCM, which differs from the classical numerical methods listed above because it is based on a random process approach and depends weakly on the dimension of the problem, providing an alternative way to deal with multidimensional problems.

Unlike the above approaches, in this paper a meshless RBF–MFS model is developed by combining radial basis function (RBF) approaches and the method of fundamental solutions (MFS) [19,20], to predict the temperature distribution in skin tissue. Firstly, the time dependence in the Pennes equation is removed by a time-stepping process and then the system is replaced by a set of inhomogeneous modified Helmholtz equations. Then, RBF approximation and the method of fundamental solution are employed to construct the particular and the homogeneous solution of the modified Helmholtz equation, respectively. The muti-subdomain method is employed to extend this model to problems with two inhomogeneous domains, such as skin with tumor, which can induce different frequencies in the modified Helmholtz equation system. The paper is organized into the following sections. In Section 2 a detailed numerical implementation is described and some important points of the proposed model are discussed. Section 3 provides some numerical examples which cover typical situations in thermal diagnostics, to demonstrate the effectiveness of the proposed method. Finally, Section 4 presents some conclusions from the presented analysis.

---

* Corresponding author. Tel.: +61 0 61258274; fax: +61 2 61250506.
  E-mail address: Qinghua.qin@anu.edu.au (Q.-H. Qin).

Nomenclature

Alphabetical symbols

c	specific heat of tissue (J/kg/°C)
c_b	specific heat of blood (J/kg/°C)
h_∞	conventional coefficient (W/m²/°C)
k	thermal conductivity of tissue (W/m/°C)
M	number of collocation points on the boundary
N_I	number of interpolation points in the domain
N_S	number of source points outside the domain
Q_m	metabolic heat of tissue (W/m³)
Q_r	spatial heating (W/m³)
Q_t	sum of metabolic heat and spatial heating (W/m³)
q	normal heat flux (W/m²)
t	time (s)
u	temperature (°C)
u_0	initial temperature (°C)
u_a	artery temperature (°C)
u_e	environmental temperature (°C)
u_w	temperature contact with probe (°C)

Greek symbols

λ	frequency of the modified Helmholtz equation

α	parameter defined in Eq. (19)
β	parameter defined in Eq. (28)
γ	parameter defined in Eq. (31)
τ	time step size
ρ	density of tissue (kg/m³)
ρ_b	density of blood (kg/m³)
ω_b	blood perfusion (m³/s/m³ tissue)
θ	temporal weighting in time-stepping method

Superscripts

1	subdomain Ω_1
2	subdomain Ω_2
n	time level n
$n + 1$	time level $n + 1$

Subscript

I	interface boundary between tissue domain and tumor domain.

2. Numerical method and algorithms

2.1. Pennes bioheat mathematical model

The well-known Pennes equation, which involves the effects of blood perfusion and metabolic heat generation, is used to simulate the thermal behaviour of biological tissue [3]:

$$\rho c \frac{\partial u(\mathbf{x}, t)}{\partial t} = \nabla \cdot [k \nabla u(\mathbf{x}, t)] + \omega_b \rho_b c_b [u_a - u(\mathbf{x}, t)] + Q_m + Q_r(\mathbf{x}, t) \tag{1}$$

where ρ, c, k are the density, specific heat, and thermal conductivity of the tissue, respectively; ω_b, ρ_b, c_b represent blood perfusion, density and specific heat of blood, respectively. u_a is the arterial temperature which is treated as constant. $u(x, t)$ is the tissue temperature; Q_m is the metabolic heat generation and $Q_r(x, t)$ is the heat source due to spatial heating. For convenience, a new symbol $Q_t(\mathbf{x}, t) = Q_r(\mathbf{x}, t) + Q_m$ including metabolic heat and special heating is introduced.

From the Pennes' equation, it can be seen that the first term on the right side represents conduction of heat in the tissue, caused by the temperature gradient. The second term describes the heat transport between the tissue and microcirculatory blood perfusion. The third term on the right depicts internal heat generation due to metabolism and the last term is spatial heating caused by external heat sources.

Practically, a rectangular area is often used in two-dimensional bioheat transfer problem (see [2,16,21]). A schematic of the 2D calculation geometry is depicted in Fig. 1.

Without losing generality, the following boundary conditions and initial condition are applied to the four boundaries to make the system complete:

• Dirichlet/necessary condition

$$u(\mathbf{x}, t) = \bar{u}(\mathbf{x}, t) \quad \in \Gamma_u \tag{2}$$

• Newman/nature condition

$$q(\mathbf{x}, t) = \bar{q}(\mathbf{x}, t) \quad \in \Gamma_q \tag{3}$$

• convective condition

$$q(\mathbf{x}, t) = h_e[u(\mathbf{x}, t) - u_e] \quad \in \Gamma_c \tag{4}$$

• initial condition

$$u(\mathbf{x}, 0) = u_0 \quad \in \Omega \tag{5}$$

where q represents the boundary normal heat flux defined as $q = -k \frac{\partial u}{\partial n}$ and n is the unit outward normal to the boundary Γ of the domain of interest Ω.

For convenience, boundary conditions (2)–(4) are expressed in a general form as

$$B_1 u(\mathbf{x}, t) + B_2 q(\mathbf{x}, t) = B_3(\mathbf{x}, t) \tag{6}$$

where B_1, B_2, and B_3 are known coefficients and can be written respectively as
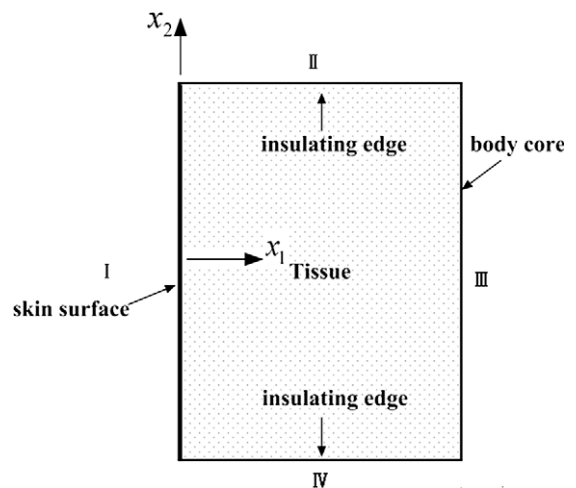

Fig. 1. Schematic diagram of computational area.

$$\begin{cases} B_1 = 1, B_2 = 0, B_3 = \bar{u} & \text{on } \Gamma_u \\ B_1 = 0, B_2 = 1, B_3 = \bar{q} & \text{on } \Gamma_q \\ B_1 = h_e, B_2 = -1, B_3 = h_e u_e & \text{on } \Gamma_c \end{cases} \tag{7}$$

2.2. Time-stepping scheme

There are two approaches in the literature for handling the time variable: (1) the Laplace transform, and (2) finite difference in time. Because numerical inversion of the Laplace transform is often ill-posed, here we apply the finite difference scheme to handle time variable. For a typical time interval $[t^n, t^{n+1}] \subset [0,T]$, $u(\mathbf{x}, t)$, its derivative with respect to time variable t and $Q_t(\mathbf{x}, t)$ are approximated as [22]:

$$\begin{aligned} u(\mathbf{x},t) &= \theta u^{n+1}(\mathbf{x}) + (1-\theta)u^n(\mathbf{x}) \\ Q_t(\mathbf{x},t) &= \theta Q_t^{n+1}(\mathbf{x}) + (1-\theta)Q_t^n(\mathbf{x}) \\ \frac{\partial u(\mathbf{x},t)}{\partial t} &= \frac{u^{n+1}(\mathbf{x}) - u^n(\mathbf{x})}{\tau} \end{aligned} \tag{8}$$

where the superscripts n and $n+1$ refer to subsequent time instances and $\tau = t^{n+1} - t^n$ is the time step size. θ ($0 \le \theta \le 1$) is a real parameter that determines whether the method is explicit ($\theta = 0$), implicit ($\theta = 1$) or a linear combination of both types [23].The special choice of $\theta = \frac{1}{2}$ is known in the literature as the Crank-Nicolson scheme.

It is easily verified that the conditions which prevent oscillation in the explicit case are exactly the same as the commonly cited sufficient conditions which ensure that it is stable. Furthermore, even though a Crank-Nicolson approach is unconditionally stable, it permits the development of spurious oscillations unless the time step size is no more than twice that required for an explicit method to be stable. Although an implicit scheme is only first-order accurate in time, it has been proved that the partial differential equation can be solved accurately using the implicit scheme [24]. Hence, we use $\theta = 1$ in our analysis.

Substituting Eq. (8) into Eqs. (1) and (6) and rearranging it gives the following modified Helmholtz-type equation that must be solved at each time step t^{n+1} for the unknown $u^{n+1}(\mathbf{x})$:

$$\begin{aligned} & u^{n+1}(\mathbf{x}) - \frac{\tau k}{\rho c}\nabla^2 u^{n+1}(\mathbf{x}) + \frac{\tau \omega_b \rho_b c_b}{\rho c}u^{n+1}(\mathbf{x}) \\ & = u^n(\mathbf{x}) + \frac{\tau \omega_b \rho_b c_b}{\rho c}u_a + \frac{\tau}{\rho c}Q_t(\mathbf{x}) \end{aligned} \tag{9}$$

$$[B_1 u^{n+1}(\mathbf{x}) + B_2 q^{n+1}(\mathbf{x})] = B_3^{n+1}(\mathbf{x}) \tag{10}$$

Note that the right-hand side of Eq. (9) is well defined in terms of the approximate solution u^n calculated on the previous time step $t = t^n$. To start the procedure we take $u(\mathbf{x}, 0) = u_0$, the initial condition of the transient bioheat problem.

For simplicity, considering the single step formula, Eq. (9) can be written as

$$(\nabla^2 - \lambda^2)u(\mathbf{x}) = f(\mathbf{x}) \tag{11}$$

where,

$$\lambda = \sqrt{\frac{\rho c}{\tau k} + \frac{\omega_b \rho_b c_b}{k}} \tag{12}$$

$$f(\mathbf{x}) = -\frac{\rho c}{\tau k}u^n(\mathbf{x}) - \frac{\omega_b \rho_b c_b}{k}u_a - \frac{Q_t}{k} \tag{13}$$

Eq. (11) is a sequence of inhomogeneous modified Helmholtz equations whose RBF–MFS solution is discussed in Sections 2.3 and 2.4 below.

2.3. RBF–MFS scheme for modified Helmholtz equations

Due to the linear property of Eq. (11), its solution can be expressed as a summation of the particular solution u_p and the homogeneous solution u_h, that is

$$u = u_p + u_h \tag{14}$$

where u_p satisfies the nonhomogenous equation

$$(\nabla^2 - \lambda^2)u_p(\mathbf{x}) = f(\mathbf{x}) \quad \mathbf{x} \in R^2 \tag{15}$$

but does not necessarily satisfy the boundary conditions (2)–(4), and u_h satisfies

$$(\nabla^2 - \lambda^2)u_h(\mathbf{x}) = 0 \quad \mathbf{x} \in R^2 \tag{16}$$

$$\begin{cases} u_h(\mathbf{x},t) = \bar{u}(\mathbf{x},t) - u_p(\mathbf{x},t) & \mathbf{x} \in \Gamma_u \\ q_h(\mathbf{x},t) = \bar{q}(\mathbf{x},t) - q_p(\mathbf{x},t) & \mathbf{x} \in \Gamma_q \\ h_\infty u_h(\mathbf{x},t) - q_h(\mathbf{x},t) = h_\infty u_\infty - h_\infty u_p(\mathbf{x},t) + q_p(\mathbf{x},t) & \mathbf{x} \in \Gamma_c \end{cases} \tag{17}$$

Similar to the treatment of Eq. (6), Eq. (17) can be written in general form,

$$[B_1 u_h(\mathbf{x}) + B_2 q_h(\mathbf{x})] = B_3(\mathbf{x}) \tag{18}$$

The particular solution u_p can be evaluated by RBF approximation [25]. To do this, the right-hand term of Eq. (15) is approximated by

$$f(\mathbf{x}) = \sum_{i=1}^{N_I} \alpha_i \varphi_i(\mathbf{x}) \quad \mathbf{x} \in \Omega \tag{19}$$

where N_I is the number of interpolation points in the domain under consideration. $\varphi_i(\mathbf{x}) = \varphi(r) = \varphi(|\mathbf{x}\text{-}\mathbf{x}_i|)$ denotes radial basis functions with reference point $\mathbf{x}_i$ and α_i are interpolating coefficients to be determined.

At the same time, the particular solution u_p is similarly expressed as

$$u_p(\mathbf{x}) = \sum_{i=1}^{N_I} \alpha_i \psi_i(\mathbf{x}) \tag{20}$$

where ψ_i represent corresponding approximated particular solutions which satisfy the following differential equations:

$$(\nabla^2 - \lambda^2)\psi_i = \varphi_i \tag{21}$$

noting the relation between the particular solution u_p and function $f(\mathbf{x})$ in Eq. (15).

By enforcing Eq. (20) to satisfy Eq. (15) at all nodes, we can obtain a set of simultaneous equations to uniquely determine the unknown coefficients α_i. In this procedure, we need to evaluate the approximate particular solutions in terms of the RBF φ. The standard approach is that φ is selected first, and then the corresponding approximate particular solutions are determined by solving Eq. (21) analytically. For the Laplace operator, ψ can be obtained by repeated integration, but for the Helmholtz-type operator this has proven difficult [26,27]. A significant result for Helmholtz-type operators was given by Chen and Rashed in which analytic formulae were given for ψ when φ was a TPS [28]:

$$\varphi = r^2 \ln r \tag{22}$$

$$\begin{cases} \psi(r) = -\frac{4}{\lambda^4} - \frac{4\ln r}{\lambda^4} - \frac{r^2 \ln r}{\lambda^2} - \frac{4K_0(\lambda r)}{\lambda^4} & r \ne 0 \\ \psi(r) = -\frac{4}{\lambda^4} + \frac{4\gamma}{\lambda^4} + \frac{4}{\lambda^4}\ln\left(\frac{\lambda}{2}\right) & r = 0 \end{cases} \tag{23}$$

where $\gamma \approx 0.5772156649015328$ is Euler's constant.

Another scheme for obtaining approximate particular solutions is a reverse approach [29,30]. Namely, ψ is first chosen directly and

then φ is evaluated from Eq. (22). For example, the particular solutions ψ are directly chosen as follows [31]:

$$\psi(r) = \frac{r^2}{4} + \frac{r^3}{9} \tag{24}$$

and the corresponding ϕ is obtained as

$$\varphi(r) = 1 + r - \lambda^2 \left(\frac{r^2}{4} + \frac{r^3}{9} \right) \tag{25}$$

It is difficult to prove mathematically under what conditions this approach is reliable, although it seems to work well so far for many problems [29,30,32].

An additional polynomial term p is required to assure nonsingularity of the interpolation matrix if the RBF is conditionally positive definite such as TPS [33,34]. And also, to achieve higher convergence rates for $f(x)$, the higher order splines are considered [35]. For example,

$$\varphi = r^{2n} \ln r \quad n \geq 1, in R^2 \tag{26}$$

Then

$$f(\mathbf{x}) = \sum_{i=1}^{N_I} \alpha_i \varphi_i^{[n]}(\mathbf{x}) + P_n \tag{27}$$

where P_n is a polynomial of total degree n. Let $\{b_j\}_{j=1}^{l_n}$ be a basis for P_n ($l_n = \begin{pmatrix} n+d \\ d \end{pmatrix}$ is the dimension of P_n; $d = 2$ for two-dimensional problems). The corresponding boundary conditions are given by

$$\sum_{i=1}^{N_I} \alpha_i b_l(P_l) = 0, \quad 1 \leq l \leq l_n \tag{28}$$

Since the inhomogeneous term $f(\mathbf{x})$ in Eq. (11) is a known function depending on the temperature field u^n, the coefficients α_i can be determined by solving Eq. (11) and Eq. (28). Then the particular solution can be obtained from Eq. (20).

The next step is to solve the homogeneous solution u_h by MFS. In the implementation of MFS, the homogeneous solution is approximated in a standard collocation fashion

$$u_h(\mathbf{x}) = \sum_{j=1}^{N_S} \beta_j u_j^*(\mathbf{x}) \tag{29}$$

where β_j are the coefficients to be determined. $u_j^*(\mathbf{x}) = u^*(|\mathbf{x} - \mathbf{x}_j|)$ are the fundamental solutions of the modified Helmholtz operator $(\nabla - \lambda^2)$. Here the source points $\{x_j\}_{j=1}^{N_S}$ are placed outside the solution domain.

Typically, for a two-dimensional problem, the fundamental solution is

$$u_j^*(\mathbf{x}) = \frac{1}{2\pi} K_0(\lambda r) \tag{30}$$

where K_0 is a modified Bessel function of the second kind with order zero.

Noting that u_h in Eq. (30) automatically satisfies the given differential Eq. (17), all we need to do is to enforce u_h to satisfy the modified boundary conditions (18) as u_p has already been calculated separately. By the collocation method, we choose the same number of collocation points as source points on the physical boundary to fit the boundary condition (18), leading to a system of linear algebraic equations in matrix form:

$$[A]\{\beta\} = \{b\} \tag{31}$$

with

$$\{\beta\} = \{\beta_1 \beta_2 \dots \beta_{N_S}\}, \quad \{b\} = \{b_1 b_2 \dots b_{N_S}\} \tag{32}$$

Once $\{\beta\}$ is obtained, u_h can be computed at any location in the domain using Eq. (29).

Additionally, the generation of source points outside the domain is a curious problem, which affects accuracy and stability. At present, there is no uniform approach to generate these source points properly. In our work, a strategy is employed [36]

$$\mathbf{y}_j = \mathbf{x}_j + \gamma(\mathbf{x}_j - \mathbf{x}_c) \tag{33}$$

where $\mathbf{x}_j$ are boundary nodes, $\mathbf{x}_c$ is the geometric center of the domain and γ is a dimensionless parameter.

Based on above operations, the complete solution $u(\mathbf{x})$ for the modified Helmholtz equation can be written as

$$u(\mathbf{x}) = \sum_{i=1}^{N_I} \alpha_i \psi_i(\mathbf{x}) + \sum_{j=1}^{N_S} \beta_j u_j^*(\mathbf{x}) \quad \mathbf{x} \in \Omega \tag{34}$$

Furthermore, the normal heat flux can be obtained as

$$q(\mathbf{x}) = -\frac{\partial u(\mathbf{x})}{\partial n} = -\sum_{i=1}^{N_I} \alpha_i \frac{\partial \psi_i(\mathbf{x})}{\partial n} - \sum_{j=1}^{N_S} \beta_j \frac{\partial u_j^*(\mathbf{x})}{\partial n} \quad \mathbf{x} \in \Omega \tag{35}$$

2.4. Multi-subdomain method for multi-material problem

As can be seen from Eq. (12), the parameter λ in the modified Helmholtz Eq. (11) depends on the material properties of the skin, such as ρ, c, w_b, ρ_b, c_b. So when the problem is a multi-material problem, λ will be different for the domain with different material and correspondingly, the modified Helmholtz equation in that domain will be different. For example, in the case of a tumor situated underneath the skin (see Fig. 2), we need to solve two different modified Helmholtz equations in each domain (the simply con-
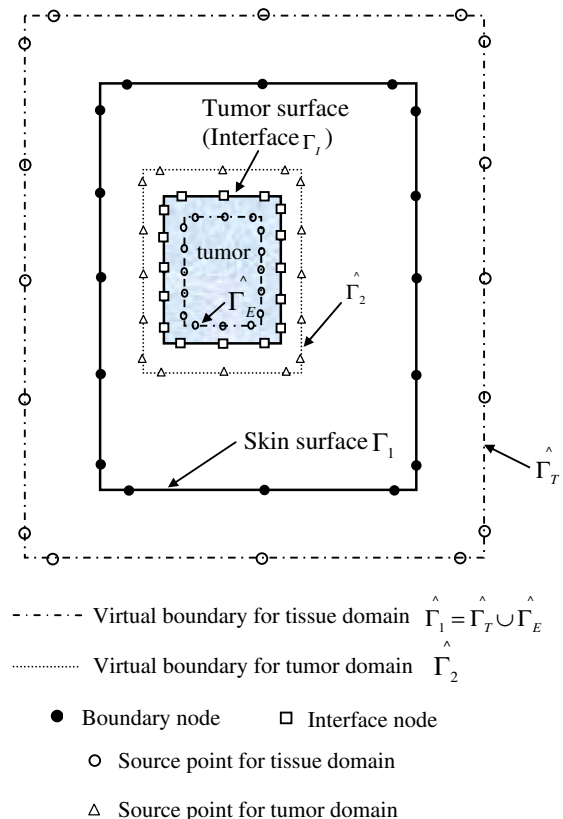

Fig. 2. Illustration of a computational domain and point discretization on the physical and virtual boundaries.

nected domain for the tumor area and the multi-connected domain for the tissue area). It should be mentioned that, unlike other multi-connected domain problems in which the boundary conditions are known on the whole multi-connected boundary, here the boundary conditions are known on the skin surface only, and are unknown on the inner boundary of the skin tissue. Moreover, the equivalences of the temperature and its normal derivative at each node of the interfaces are required to satisfy the continuity on the interface between tissue and tumor. In addition, it should be mentioned that the continuity condition is for the total value of u ($=u_p + u_h$), whereas Eqs. (36) and (37) below are for u_h only. This leads to the complex form of Eqs. (39) and (40). Based on the discussion above, we propose the multi-subdomain method for the application of MFS in the interface condition between two different material domains in the following.

In the multi-subdomain method, the solution domain is divided into the two subdomains Ω_1 and Ω_2, where Ω_1 represents the tissue domain and Ω_2 the tumor domain. In Fig. 2, boundaries Γ_1 and Γ_I denote respectively the real boundaries of the skin surface and the interface between skin tissue and tumor. For the multi-connected tissue domain Ω_1, $2M$ source nodes are placed on two auxiliary surfaces ($\hat{\Gamma}_1 = \hat{\Gamma}_T \cup \hat{\Gamma}_E$) which are determined by inflation/deflation of the tissue surfaces (skin surface and interface), where M is the number of collocation points on the boundary. The virtual boundary corresponding to the skin surface $\hat{\Gamma}_T$ and interface $\hat{\Gamma}_E$ is obtained by scaling the skin surface and interface with the factor γ in Eq. (33) as 1.2 and −0.8 respectively. For the single connected tumor domain Ω_2, M source nodes are placed on one auxiliary surface ($\hat{\Gamma}_2$) which is determined by inflation of the tumor surface (interface, see Fig. 2).

In the MFS formulation for the tissue domain Ω_1, we have

$$[A^1]\{\beta^1\} = \{b^1\} \tag{36}$$

For the tumor domain Ω_2, we have

$$[A^2]\{\beta^2\} = \{b^2\} \tag{37}$$

where the superscripts 1 and 2 stand for variables associated with the subdomains Ω_1 and Ω_2, respectively.

On the interface boundary Γ_I, the following conditions must be satisfied:

$$\{u_I^1\} = \{u_I^2\} = \{u_I\}$$
$$\{q_I^1\} = -\{q_I^2\} = \{q_I\} \tag{38}$$

where subscript 'I' represents the interface boundary between the tissue domain and the tumor domain.

Rearranging the elements of the matrices and vectors in Eqs. (36) and (37) and making use of Eq. (38) yields

$$
\begin{bmatrix} A_1^1 \\ A_{Iu}^1 \\ A_{Iq}^1 \end{bmatrix}_{3M \times 2M} [\beta^1]_{2M \times 1} = \begin{Bmatrix} b_1^1 - b_{p1}^1 \\ u_I^1 - u_{p1}^1 \\ q_I^1 - q_{p1}^1 \end{Bmatrix}_{3M \times 1} = \begin{Bmatrix} b_1^1 - b_{p1}^1 \\ u_I - u_{p1}^1 \\ q_I - q_{p1}^1 \end{Bmatrix}_{3M \times 1} \tag{39}
$$

$$
\begin{bmatrix} A_{Iu}^2 \\ A_{Iq}^2 \end{bmatrix}_{2M \times M} [\beta^2]_{M \times 1} = \begin{Bmatrix} u_I^2 - u_{p2}^2 \\ q_I^2 - q_{p2}^2 \end{Bmatrix}_{2M \times 1} = \begin{Bmatrix} u_I - u_{p2}^2 \\ -q_I - q_{p2}^2 \end{Bmatrix}_{2M \times 1} \tag{40}
$$

where the subscripts u and q denote respectively the boundary conditions on which temperature u and heat flux q are known.

Collecting the terms with the same variable in Eqs. (39) and (40) above and rearranging them, we have

$$
\begin{bmatrix} A_1^1 & 0 \\ A_{Iu}^1 & -A_{Iu}^2 \\ A_{Iq}^1 & A_{Iq}^2 \end{bmatrix}_{3M \times 3M} \begin{bmatrix} \beta^1 \\ \beta^2 \end{bmatrix}_{3M \times 1} = \begin{Bmatrix} b_1^1 - b_{p1}^1 \\ -u_{p1}^1 + u_{p2}^2 \\ -q_I^1 - q_{p2}^2 \end{Bmatrix}_{3M \times 1} \tag{41}
$$

It can then be further written as

$$[A]\{\beta\} = \{b\} \tag{42}$$

from which all unknown coefficients $\{\beta\}$ can be determined. Further, the temperature field at any point within the domain can be evaluated from Eq. (34)

3. Numerical examples

Here we consider four cases of transient heat transfer in skin tissue. The four cases cover normal tissue, tissue with tumor and burned tissue. It should be mentioned here that the purpose of these examples is to provide an insight into performance and the applicability of the proposed numerical method, the computational model is, therefore, not physiologically realistic.

In the following computation, typical tissue properties including $\rho = \rho_b = 1000\ \text{kg/m}^3$, $c = c_b = 4000\ \text{J/(kg °C)}$, $k = 0.5\ \text{W/(m °C)}$, $u_a = 37\ °C$, $u_c = 37\ °C$ and $u_0 = 37\ °C$ are employed [2]. As time iteration is required in the algorithm, the convergence criterion for determining the final steady-state is set as

$$|u^{n+1} - u^n| \leq 10^{-3} \tag{43}$$

3.1. Rectangular domain of solid subjected to temperature impact

For the purpose of validating the program, a benchmark example of a rectangular domain subjected to temperature impact is considered. Referring to Fig. 1, the entire body has a width of 0.03 m along the x_1 direction and a length of 0.08 m along the x_2 direction. The boundary conditions are:

$$u(x_1, x_2; t) = u_s = 45\ °C, \quad x_1, x_2 \in I$$

$$q(x_1, x_2; t) = 0, \quad x_1, x_2 \in II, IV$$

$$u(x_1, x_2; t) = u_c = 37\ °C, \quad x_1, x_2 \in III$$

The initial condition is $u(x_1, x_2; 0) = 33\ °C$, $x_1, x_2 \in \Omega$.

The steady-state analytical solution without metabolic heat of the rectangular domain is given by [37]

$$u(x_1) = u_a + \frac{(u_s - u_a)\sinh[\mu(L - x_1)] + (u_c - u_a)\sinh(\mu x_1)}{\sinh(\mu L)} \tag{44}$$

with $\mu = \sqrt{\omega_b \rho_b c_b / k}$.

As stated above, the purpose of this example is to assess the efficiency of the proposed scheme with respect to different RBF schemes (standard approach and reverse approach) and time increment τ. Moreover, for the standard approach, splines with dif-

Table 1
Comparison of absolute maximum error ($\times 10^{-2}$) by different particular solutions in RBF.

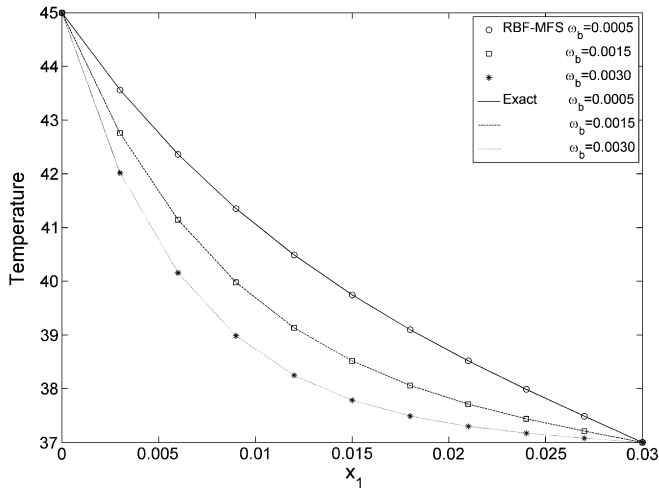| τ	S1	S2	S3	S4	PS1	PS2	PS3	PS4	Inverse method
100	6.835	6.928	6.851	6.881	6.908	6.887	6.966	6.857	6.885
500	6.849	6.908	6.855	6.866	6.858	6.862	6.881	6.856	6.900
1000	6.851	6.891	6.856	6.862	6.862	6.859	6.870	6.856	6.894
2000	6.853	6.880	6.857	6.859	6.859	6.858	6.863	6.857	7.694

Fig. 3. Steady-state temperature distribution along the depth of skin for different blood perfusion rate.
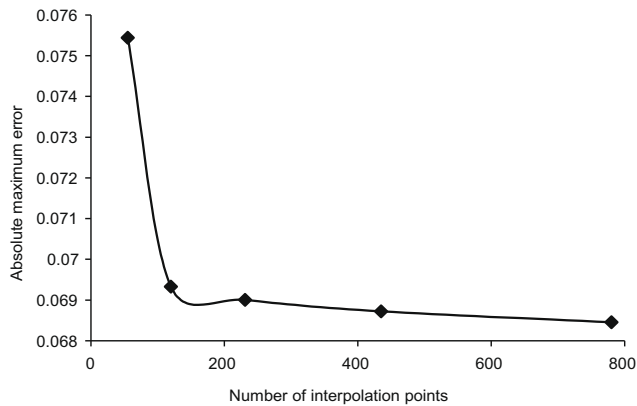

Fig. 4. Absolute maximum error using different interpolation points.
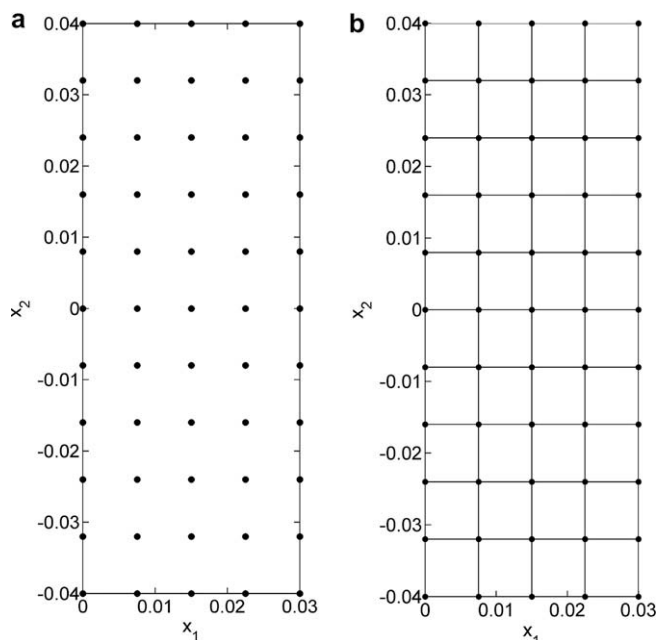

Fig. 5. (a) Profile of interpolation points for RBF–MFS. (b) Mesh division for Trefftz FEM.

ferent orders are considered. In Table 1, Si (i = 1–4) denote the results obtained by using splines $\varphi = r^{2i} \ln r$ in Eq. (19) and without additional polynomial terms. For comparison purposes, PSi (i = 1–4) denote the results obtained by using Eq. (27) with additional polynomial terms p_i.

Although the numerical results in Table 1 show that the standard method is more accurate than inverse method except for τ = 100, the inverse method can save considerable computing time, as calculating the modified Bessel function is quite complex and time-consuming. For orders 1 and 3, adding an additional polynomial term can increase the accuracy, but for orders 2 and 4 the reverse is observed. In general, the results improve with higher order polyharmonic splines and reduced time steps, but this is not always the case. Although more accurate results can be obtained by using higher order polyharmonic splines for elliptic boundary value problems, from the above results we see limited improvement in time-dependent problems presumably because the dominant error was caused by the time-stepping scheme. Moreover, the higher order polyharmonic splines result in inferior conditioning of the linear system associated with the homogeneous solution. Considering these factors, in the following numerical simulation we choose time step τ = 500 and the inverse method which can reduce the computing time dramatically. In Fig. 3, which shows the final steady-state temperature along the depth of skin tissue under the applied surface temperature, it can be seen that the results agree well with the exact ones. Furthermore, to investigate the influence of blood perfusion on temperature distribution in the living tissue, the simulation is also applied to different value of ω_b (ω_b = 0.0005, 0.0015, 0.0030 ml³/s/ml³). Fig. 3 shows that the effect of blood perfusion rate on temperature distribution is significant. A larger blood perfusion rate results in a quick drop in the tissue temperature. This is reasonable as larger blood perfusion rates can carry away more heat. In addition, to assess the convergent performance of the model, different numbers of internal interpolation points in the domain, 55, 120, 231, 435 and 780, are employed in the calculation (w_b = 0.0005 is used here and same after). Fig. 4 shows the absolute maximum error using different interpolation points. As expected, the results gradually converge to the exact values along with the increase in the number of interpolation points. Moreover, to evaluate the merit of the proposed method, calculations have also been conducted using Trefftz finite element method. The element mesh used in the calculation is shown in Fig. 5b, whose number of nodes is the same as those used in RBF–MFS (see Fig. 5). The convergent result is achieved at t = 7500 s in terms of the analytical solution. It can also be seen from Table 2 that the proposed meshless method can achieve higher accuracy than Trefftz FEM on the specified points and the average relative error for the whole domain is 2.2167e−2 and 2.8192e−2 for RBF–MFS meshless method and Trefftz FEM, respectively (the average relative error on a variable f is introduced as $Arerr(f) =$
$$\sqrt{\frac{\sum_{i=1}^{N}(f_{num}-f_{ana})_i^2}{\sum_{i=1}^{N}(f_{ana})_i^2}}).$$ It indicates that the proposed meshless method can achieve higher accuracy than that from Trefftz FEM. Furthermore, the proposed algorithm is easy to implement into the standard computer program.

Table 2
Comparison of the results from the two numerical methods.

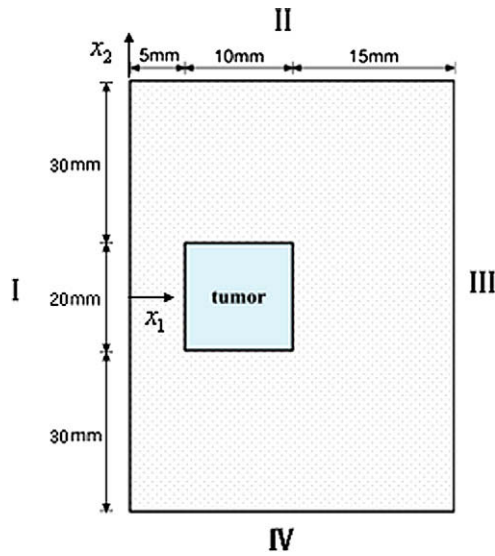| X_1	0.0000	0.0075	0.0150	0.0225	0.0300	Arerr for whole domain
Analytical solution	45.0000	40.4973	38.4912	37.5495	37.000	
RBF–MFS	45.0000	41.8241	39.7267	38.2579	37.000	2.2167e−2
Trefftz FEM	45.0000	42.7443	40.8305	39.1767	37.000	2.8192e−2

Fig. 6. Illustration of tissue with tumor.

3.2. Tumor hyperthermia

It is known that the distribution of both blood perfusion and metabolic heat generation is affected by the presence of a tumor [2]. The distribution of temperature at the skin surface is different from the normal distribution. It is a benefit that this difference can be used for non-invasive diagnostics of the physiological stage of the biological body. In this example, a vascularised tumor situated beneath the skin demonstrates that benefit. The calculation model is taken from Ref. [2]. Fig. 6 shows the size and location of the tumor. The boundary conditions are:

$$q(x_1, x_2; 0) = 0, \quad x_1, x_2 \in I, II, IV$$

$$u(x_1, x_2; 0) = 37^\circ C, \quad x_1, x_2 \in III$$

and $\omega_b = 0.0005 \text{ m}^3/\text{s/m}^3, Q_m = 420 \text{ W/m}^3$ for healthy tissue

$$\omega_b = \begin{cases} 0.0005 \text{m}^3/\text{s/m}^3 & x_1, x_2 \notin L \\ 0.002 \text{m}^3/\text{s/m}^3 & x_1, x_2 \in L \end{cases}$$

- ● field nodes on real boundary
- ○ source nodes for healthy tissue domain
- + interpolation nodes over healthy tissue domain
- × interpolation nodes over tissue domain
- □ field nodes on interface
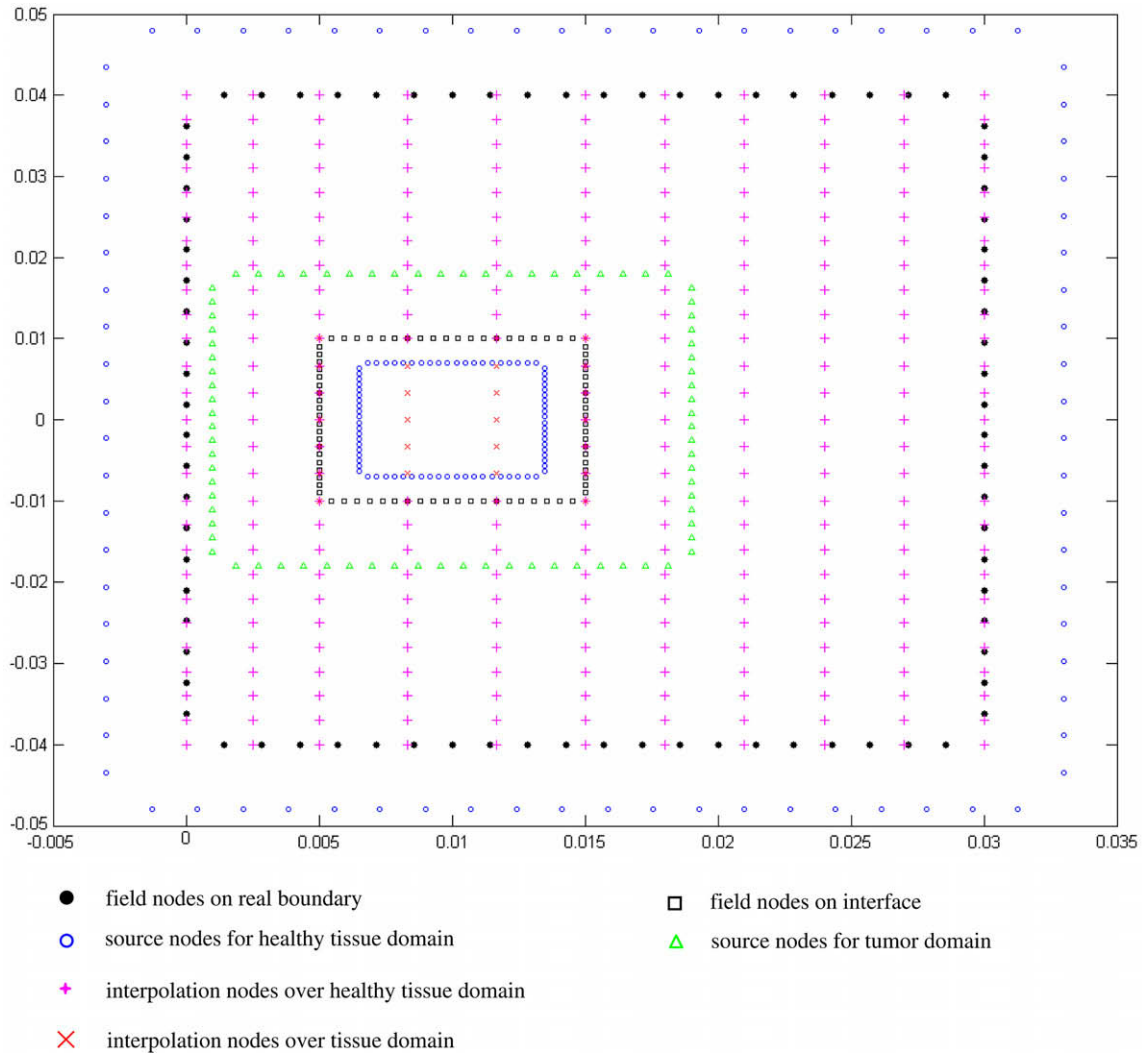- △ source nodes for tumor domain

Fig. 7. Demonstration of virtual source points, collocations and interpolation points.

$$Q_m = \begin{cases} 420\,\text{W/m}^3 & x_1, x_2 \notin L \\ 4200\,\text{W/m}^3 & x_1, x_2 \in L \end{cases}$$

for tissue with a tumor, where $L \subseteq [|x_2| \leq 0.01\,\text{m}, 0.005\,\text{m} \leq x_1 \leq 0.015\,\text{m}]$ is prearranged as the tumor domain.

The multi-subdomain formulation given in Eq. (41) is employed to predict the temperature distribution in both healthy tissue and the tumor domain. In the calculation, 80 field nodes on the real boundary and 287 uniform distributed interpolation nodes within the solution domain are used. Further, 80 field nodes are placed on the interface, 160 source nodes over the healthy tissue domain, and 80 source nodes over the tumor domain, as shown in Fig. 7. Fig. 8 shows the spatial temperature profiles for both healthy tissue and tumor tissue. As expected, the temperature distribution in the tumor tissue is higher than that in the healthy skin, due to the increased blood perfusion and metabolic heat generation caused by the tumor. Additionally, the temperature of the skin over the tumor is found to be several degrees higher than that of the surrounding area. This difference can serve as a clinical sign for tumor detection. Fig. 9 shows a comparison of the skin temperature of two types of tissue. The trend matches well with the results in reference [2].

3.3. Detection of skin burn injury

Skin burn is caused by the accidents such as fire exposure, contact with objects which have an extremely high temperature, electricity, harmful radiation, etc. Accurate early assessment of skin damage in a burn injury can greatly improve subsequent care [2]. Therefore, it is necessary to develop a quick and convenient numerical way to simulate, detect and evaluate the harmful skin burn injury. In this example, comparison of different responses of burned skin with normal skin is illustrated by imposing spatial heating such as a low power of laser radiation to analyse the detection of skin burns. Referring to Fig. 1, the domain has a 0.004 m width in the x_1 direction and 0.008 m length in the x_2 direction. The boundary conditions are:

$$q(x_1, x_2; t) = h(u - u_\infty) \quad x_1, x_2 \in I$$

$$q(x_1, x_2; t) = 0, \quad x_1, x_2 \in II, IV$$
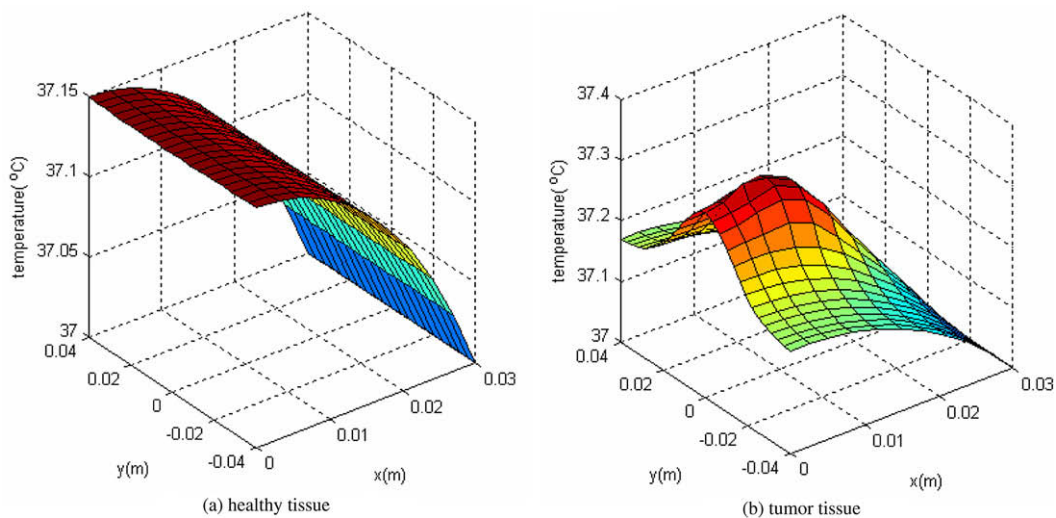
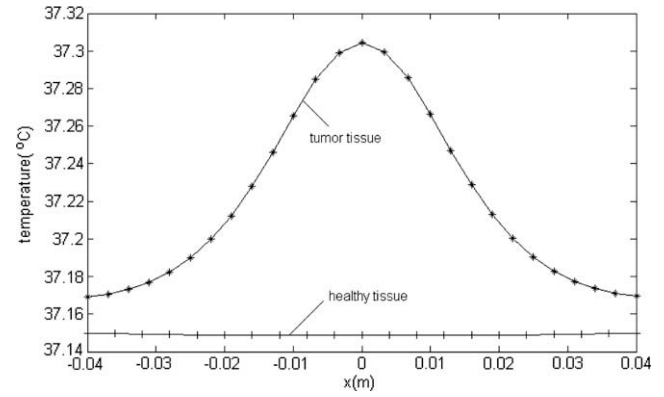$$u(x_1, x_2; t) = 33^\circ C, \quad x_1, x_2 \in III$$

Fig. 9. Skin temperature of two types of tissue.

The initial condition is $u(x_1, x_2; 0) = 33\,^\circ\text{C}$, $x_1, x_2 \in \Omega$ and the function for the laser radiation used is $Q_r = \beta I(t)e^{-\beta\sqrt{x_1^2+x_2^2}} = \beta I_0 e^{-\beta\sqrt{x_1^2+x_2^2}}$ [38]. Other properties used are: $\rho_0 c_0 = 3.96 \times 10^6$ J/m^3 K, $\beta = 700$, $I_0 = 500$ w/m^3, $h = 10$ W/m^2 K, $u_\infty = 33\,^\circ$C.

Moderate laser radiation is applied to the surface of the skin including both healthy and burned skin. Heat conduction and blood perfusion for normal tissue are assumed to be $k = 0.425$ W/m $^\circ$C and $\omega_b = 0.0005$ ml/s/ml respectively. In comparison, the lower values of heat conduction and blood perfusion used for burned tissue are $k = 0.235$ W/m $^\circ$C and $\omega_b = 0.0001$ ml/s/ml, respectively.

Fig. 10 shows the spatial temperature profiles for normal tissue and burned tissue. The larger amplitude for the temperature in burned tissue is the result of the loss of water in the tissue and destruction of the vascular bed in burned tissue.

4. Conclusion

A RBF–MFS algorithm was developed for analysing transient two-dimensional bioheat transfer problems. A special multi-domain MFS formulation was presented to handle multi-material and multi-connected domain problems using RBF–MFS formulation. It should be mentioned that, unlike the traditional domain decomposition method in which the boundary conditions are known on the whole multi-connected boundary, the boundary conditions are here known on the skin surface only, and are unknown on the inner boundary of the skin tissue. Moreover, it
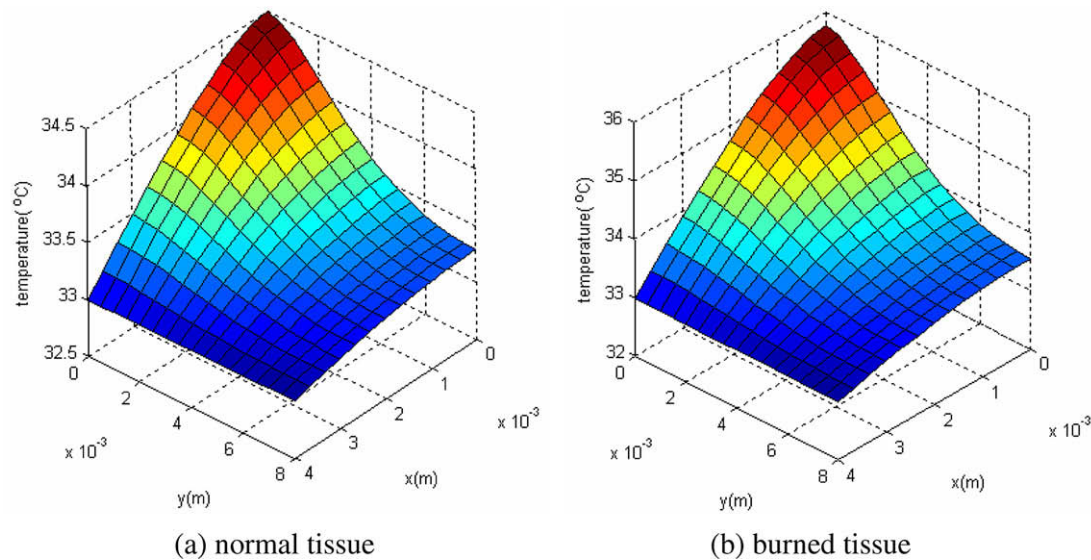

Fig. 8. Steady state temperature distributions of healthy and tumor tissue.

(a) normal tissue   (b) burned tissue

Fig. 10. Steady state temperature distribution in normal and burned tissue.

should be mentioned that the continuity condition over the interface between two domains with different materials is for the total value of u (=u_p + u_h), whereas Eqs. (36) and (37) are for u_h only. As a result, the complex forms of Eqs. (39) and (40) are induced. To illustrate applications of the proposed methods, several typical examples often occurred in therapeutic treatment are considered, which include normal tissue, tissue with tumor, and burned tissue. The results show that the proposed method is an efficient meshfree method, which is easy to understand, has a simple solution procedure, high accuracy, and stability, and can analyse thermal behaviour of inhomogeneous materials.

References

[1] M. Miyakawa, J.C. Bolomey, Non-Invasive Thermometry of the Human Body, CRC Press, 1996.

[2] J. Liu, L.X. Xu, Boundary information based diagnostics on the thermal states of biological bodies, Int. J. Heat Mass Transfer 43 (2000) 2827–2839.

[3] H.H. Pennes, Analysis of tissue and arterial blood temperatures in the resting human forearm, J. Appl. Physiol. 1 (1948) 93–122 (August 1).

[4] J.J. Zhao, J. Zhang, N. Kang, F. Yang, A two level finite difference scheme for one dimensional pennes' bioheat equation, Appl. Mathe. Comput. 171 (2005) 320–331.

[5] J. Nadobny, M. Szimtenings, D. Diehl, E. Stetter, G. Brinker, P. Wust, Evaluation of mr-induced hot spots for different temporal sar modes using a time-dependent finite difference method with explicit temperature gradient treatment, IEEE Trans. Biomed. Eng. 54 (2007) 1837–1850.

[6] M.R. Rossi, D. Tanaka, K. Shimada, Y. Rabin, An efficient numerical technique for bioheat simulations and its application to computerized cryosurgery planning, Comput. Meth. Program. Biomed. 85 (2007) 41–50.

[7] I. Chatterjee, R.E. Adams, Finite element thermal modelling of the human body under hyperthermia treatment for cancer, Int. J. Comput. Appl. Technol. 7 (1994) 151–159.

[8] D.A. Torvi, J.D. Dale, A finite element model of skin subjected to a flash fire, J. Biomechan. Eng. 116 (1994) 250–255.

[9] P.M. Meaney, R.L. Clarke, G.R. ter Haar, I.H. Rivens, A 3D finite-element model for computation of temperature profiles and regions of thermal damage during focused ultrasound surgery exposures, Ultrasound Med. Biol. 24 (1998) 1489–1499.

[10] G. Zhao, H.F. Zhang, X.J. Guo, D.W. Luo, D.Y. Gao, Effect of blood flow and metabolism on multidimensional heat transfer during cryosurgery, Med. Eng. Phys. 29 (2007) 205–215.

[11] P. Yuan, H.E. Liu, C.W. Chen, H.S. Kou, Temperature response in biological tissue by alternating heating and cooling modalities with sinusoidal temperature oscillation on the skin, Int. Commun. Heat Mass Transfer 35 (2008) 1091–1096.

[12] E.H. Ooi, W.T. Ang, E.Y.K. Ng, Bioheat transfer in the human eye: a boundary element approach, Eng. Anal. Bound. Elem. 31 (2007) 494–500.

[13] C.L. Chan, Boundary element method analysis for the bioheat transfer equation, J. Biomechan. Eng. 114 (1992) 358–365.

[14] W.Q. Lu, J. Liu, Y. Zeng, Simulation of the thermal wave propagation in biological tissues by the dual reciprocity boundary element method, Eng. Anal. Bound. Elem. 22 (1998) 167–174.

[15] Z.S. Deng, J. Liu, Monte carlo method to solve multidimensional bioheat transfer problem, Numer. Heat Transfer, B 42 (2002) 543–567.

[16] Z.S. Deng, J. Liu, Mathematical modeling of temperature mapping over skin surface and its implementation in thermal disease diagnostics, Comput. Biol. Med. 34 (2004) 495–521.

[17] J. Jirousek, Q.H. Qin, Application of hybrid-trefftz element approach to transient heat conduction analysis, Comput. Struct. 58 (1996) 195–201.

[18] Q.H. Qin, Trefftz finite and boundary element method, WIT Press, Southampton, 2000.

[19] H. Wang, Q.H. Qin, Y.L. Kang, A meshless model for transient heat conduction in functionally graded materials, Comput. Mechan. 38 (2006) 51–60.

[20] H. Wang, Q.H. Qin, Y.L. Kang, A new meshless method for steady-state heat conduction problems in anisotropic and inhomogeneous media, Arch. Appl. Mechan. 74 (2005) 563–579.

[21] Z.S. Deng, J. Liu, Parametric studies on the phase shift method to measure the blood perfusion of biological bodies, Med. Eng. Phys. 22 (2000) 693–702.

[22] R. Chapko, R. Kress, Rothe's method for the heat equation and boundary integral equations, J. Int. Eq. Appl. 9 (1997) 47–69.

[23] J.W. Thomas, Numerical Partial Differential Equations Illustrated, Springer, 1995.

[24] R. Zvan, K.R. Vetzal, P.A. Forsyth, PDE methods for pricing barrier options, J. Econom. Dynam. Control 24 (2000) 1563–1590.

[25] M. Golberg, Recent developments in the numerical evaluation of particular solutions in the boundary element method, Appl. Mathe. Comput. 75 (1996) 91–101.

[26] M. Golberg, C. Chen, The theory of radial basis functions applied to the BEM for inhomogeneous partial differential equations, Bound. Elem. Commun. 5 (1994) 57–61.

[27] M. Golberg, C. Chen, J. Fromme, Discrete Projection Methods For Integral Equations, Computational Mechanics Publication, Southampton, 1997.

[28] C.S. Chen, Y.F. Rashed, Evaluation of thin plate spline based particular solutions for helmholtz-type operators for the DRM, Mechan. Res. Commun. 25 (1998) 195–201.

[29] L.C. Wrobel, D.B. DeFigueiredo, A dual reciprocity boundary element formulation for convection-diffusion problems with variable velocity fields, Eng. Anal. Bound. Elem. 8 (1991) 312–319.

[30] N.A. Schclar, Anisotropic Analysis Using Boundary Elements, WIT Press, Southampton, 1994.

[31] K. Balakrishnan, R. Sureshkumar, P.A. Ramachandran, An operator splitting-radial basis function method for the solution of transient nonlinear poisson problems, Comput. Mathe. Appl. 43 (2002) 289–304.

[32] M. Kogl, L. Gaul, Dual reciprocity boundary element method for three-dimensional problems of dynamic piezoelectricity, Eng. Anal. Bound. Elem. 8 (1999) 312–319.

[33] E.J. Kansa, Multiquadrics – a scattered data approximation scheme with applications to computational fluid-dynamics – ii solutions to parabolic, hyperbolic and elliptic partial differential equations, Comput. Mathe. Appl. 19 (1990) 147–161.

[34] M. Zerroukat, H. Power, C.S. Chen, A numerical method for heat transfer problems using collocation and radial basis function, Int. J. Numer. Meth. Eng. 42 (1998) 1263–1278.

[35] A.S. Muleshkov, M.A. Golberg, C.S. Chen, Particular solutions of helmholtz-type operators using higher order polyhrmonic splines, Comput. Mechan. 23 (1999) 411–419.

[36] D.L. Young, S.J. Jane, C.M. Fan, K. Murugesan, C.C. Tsai, The method of fundamental solutions for 2d and 3d stokes problems, J. Comput. Phys. 211 (2006) 1–8.

[37] H.S. Carslaw, J.C. Jaeger, Conduction of Heat in Solids, second ed., Oxford University Press, Berlin, USA, 1986.

[38] L. Autrique, C. Lormel, Numerical design of experiment for sensitivity analysis & application to skin burn injury prediction, IEEE Trans. Biomed. Eng. 55 (2008) 1279–1290.